Probabilistic prediction of the size effect on the fatigue strength

for variable length specimens of selective laser melted 316L stainless steel

Tomasz Tomaszewski[*], Andrzej Skibicki

Faculty of Mechanical Engineering, University of Science and Technology,

al. Prof. S. Kaliskiego 7, 85-796 Bydgoszcz, Poland

Abstract

The paper presents an approach for modelling of the size effect in the high-cycle fatigue for an additively manufactured stainless steel. The analyses verify the probability of a critical defect, significantly speeding up fatigue crack initiation. An assessment of the fracture surface failure mechanism shows the presence of a void due to lack of fusion. The selected defect parameters significantly decrease the fatigue strength with increasing specimen length. The implemented linear model of the normalized Crossland stress provides a good fit to the experimental data. The probabilistic approach to the scatter of the selected variables shows the correct prediction of fatigue properties.

Keywords

Nomenclature

$\sqrt{area}$	Murakami defect size parameter
$\sqrt{area}_0$	material constant of Murakami parameter
μ_0	normal distribution size parameter
d_l	defect type parameter
F	axial force
HV	Vickers hardness
$J_{1,max}$	max. hydrostatic stress over a loading cycle
$J_{2,a}$	amplitudes of a second invariant of a deviatoric stress tensor over a loading cycle
K_t	theoretical stress concentration factor
l_s	overall specimen length
l_w	length of specimen working part
m, b	linear regression coefficients

[*]Corresponding author:
E-mail address: tomaszewski@pbs.edu.pl

n	number of specimens
$n\%$	highly stressed parameter
n_d	number of defects
N_f	number of cycles to failure
P	probability
P_f	failure probability
R	stress ratio
R^2	determination coefficient
R_f	radius of fillet
S_f	fatigue strength
$S_{f,est}$	estimated fatigue strength
$S_{f,n}$	normalized fatigue strength
$S_{f,pred}$	predicted fatigue strength
S_{max}	maximum normal stress
t_b	min. thickness between a specimen outer surface and defect
t_d	max. thickness between a specimen outer surface and defect
$V_{n\%}$	highly stressed volume
α	Weibull distribution shape parameter
α_0	significance level of a confidence interval
α_{CR}, β_{CR}	material parameters of the Crosslands criterion
α_M	exponent of the Murakami model
$\beta_0 - \beta_5$	non-linear regression coefficients
δ	Weibull distribution scale parameter
δ_p	relative error
ΔS_f	fatigue strength range
$\Delta S_{f,0}$	upper limit of fatigue strength range
λ	Weibull distribution location parameter
ρ_d	defect density
σ_0	normal distribution shape parameter
σ_{CR}	Crossland equivalent stress

$\sigma_{CR,n}$ normalized Crossland equivalent stress

σ_{max} max. normal stress

σ_w fatigue strength at a knee point of fully reversed tension/compression

τ_w fatigue strength at a knee point of fully reversed torsion

1. Introduction

The fatigue failure tests are generally carried out on a selected object size, resulting in limited assessment and extrapolation of data beyond the experimental test conditions. The physical difficulties of testing objects at full scale, and the technical and financial constraints, necessitate the testing of small size specimens. Transferring experimental data to a full scale structure requires determination of the size effect on fatigue properties. Commonly used recommendations and guidelines contain empirical relationships based on correcting factors [1-3].

The size effect prediction models are categorised according to the factors selected [4]. The statistical approach assumes a random material defect independent of the object size [5]. The increase in the number of defects causing fatigue crack initiation and propagation is proportional to the object size, decreasing the fatigue strength. The weakest link theory defines statistically located defects in a unit of material [6]. The crack initiates in a limited volume containing a critical defect or the weakest link in the material. The local failure probability is related to the global failure probability of the structure. An increase in the size effects determines an increase in the data scatter, described by the location parameter of the Weibull distribution [7].

The effect of inhomogeneous stress distribution and specimen size on fatigue properties is modelled deterministically using a volumetric model. The geometric approach related to the stress gradient is noted under loading conditions of bending or torsion and axial loading of discontinuous geometrically notched objects. The model defines a highly stressed volume [8, 9] or surface [10-12]. The probability of crack initiation or enlargement of an existing defect in this region is higher. The local volume or surface is loaded with at least n% of the maximum stress. The combination of this model with the weakest link theory provides a prediction of probabilistic scatter bands [13].

The fatigue life for a constant stress range is random. Therefore, a correct analysis of this phenomenon requires the implementation of a probabilistic model without arbitrary assumptions about its functional form [14]. A parametric function using statistical assumptions determines the modelling for the failure probability distribution of the selected random variable. The asymptotic function for implementing the variable lower limit assumption is the Weibull distribution [6, 15]. The methods based on a strictly statistical approach do not accurately represent the fatigue failure mechanism [16]. The probabilistic modelling of the phenomenon requires linking a random

variable for a selected statistical distribution to a defined measure of material failure, as presented in the papers [17, 18].

The paper presents an attempt to model the size effect from experimental observations of selected random variables affecting the fatigue behaviour of a selective laser melted 316L stainless steel. The applied generalisations and simplifications of the procedures for predicting fatigue properties are the result of considering significant factors on the analysed phenomenon, including modelling limitations not resulting from the assumptions of the implemented approaches. The material defect formed during additive manufacturing determines the failure mechanism. The probabilistic approach defines the defect parameter in a highly stressed volume according to the weakest link theory. The output data is the fatigue strength related to the failure probability. The result for a variable specimen size is predicted using extreme value statistics and the Kitagawa-Takahashi diagram to approximate the fatigue strength. The specimens are disproportionately modified in relation to the geometric dimensions of the reference specimen. The analysed dimensional relationship is observed in objects of variable length [19, 20].

2. Experimental methods

2.1. Material

The material tested is additive manufactured 316L stainless steel. The powder was produced by atomising the material in an argon atmosphere. The grain size of the powder was analysed using a scanning electron microscope (Fig. 1). The material consists of spherical grains. The average size is 44.8 µm. The general chemical composition has been summarised as a percentage by weight: 0.03 C; 1.00 Si; 2.00 Mn; 0.03 S; 0.04 P; 16-18 Cr; 10-14 Ni; 2-3 Mo.

The specimens were manufactured by laser powder bed fusion (PBF-LB) technology using a selective laser melting process. The three-dimensional models of the specimens in STL format were used to prepare a laser scan path with a power of 200 W, a scan speed of 800 mm/s, a hatching pitch of 0.12 mm and a layer thickness of 0.03 mm. The additive manufacturing was carried out on the SLM 125HL machine under argon gas shielding. The powder melt path was non-unidirectional oriented stress. The constant manufacturing parameters were used for all specimens. There was no further heat treatment applied. Fig. 2 shows an example view of the specimens on the build plate. The geometry of the fatigue test specimens is given in Section 2.2.
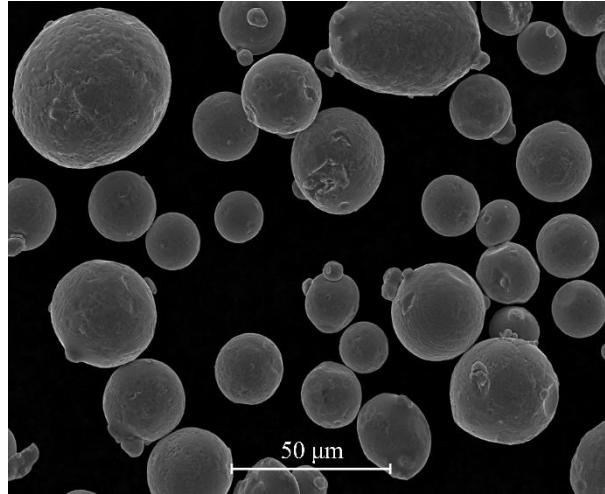
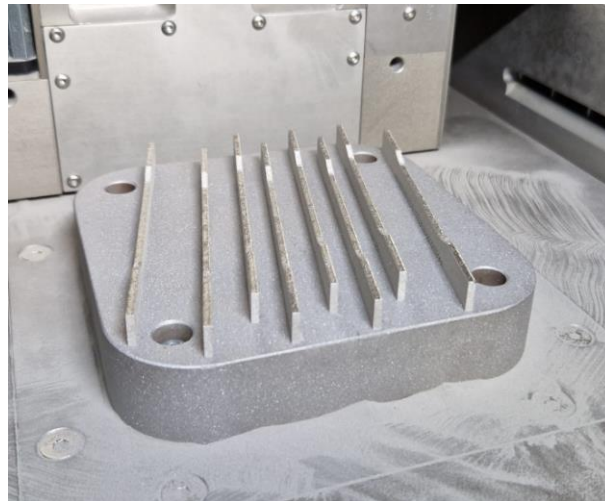Fig. 1. SEM image of powder made from 316L stainless steel.

Fig. 2. Selected view of specimens on the build plate of the SLM 125HL machine.

The microstructure of the as-built material was analysed in a plane perpendicular (x-z) to the build plate. This plane, built up layer by layer during additive manufacturing, contains the thermal history of the process. The final surface of the specimen was polished and etched in an acetic glyceregia. Fig. 3a shows an example of an optical micrograph of a polished surface. The pointed black areas represent pores. The visible material defects are characterised by irregular shape and variable size. The porosity is not uniform. The additive manufacturing process of the PBF-LB 316L stainless steel causes randomly distributed pores. A few clusters of smaller pores and larger defects can be observed under the top layer of the material. The selected subsurface defects can generate a stress state that significantly affects fatigue crack initiation [21]. A detailed analyses are provided in Section 3.2.
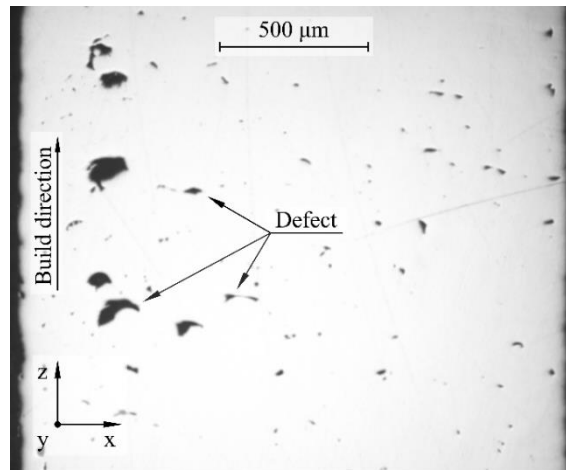
(a)
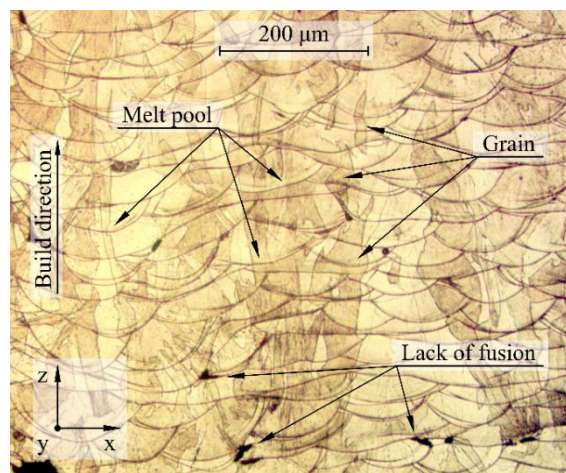
(b)

Fig. 3. Optical micrographs of the PBF-LB 316L stainless steel in the plane perpendicular (x-z) to the build plate: a) polished material showing porosity, b) as-built, etched material.

Fig. 3b shows an optical microscopic analysis of a selected area of the etched surface. The clearly visible boundaries of the melt pools represent the solidification pattern during the PBF-LB process, along the heat gradient from the edge to the core. The pointed pores define the insufficient overlap of the melt pools, resulting in a lack of fusion between the layers. The observed microstructural inhomogeneity may be due to process inaccuracies, non-uniformity of the melt pool, impurities, inclusions and spatter. The elongated shape of the grains is oriented along the build direction (z-axis) through the boundaries of the melt pools. The epitaxial solidification of layers along the thermal gradient result in columnar, vertical grains. The microstructures identified are features commonly found in the selective laser melted 316L stainless steel [22-24].

The mechanical properties were determined by a static tensile test according to ISO 6892 [25] using a flat smooth specimen (length of working part – 15 mm, thickness – 2 mm, minimum width – 4 mm, radius of fillet – 12 mm). The specimens were additively manufactured along the z-axis. The working part at the specimen thickness

was machined due to the removal of supports. The constant machining parameters were applied to both symmetrical specimen surfaces. There was no additional surface finish applied. All experimental tests were carried out on an Instron 8874 materials testing machine, equipped with a ± 25 kN force gauge and an Instron 2620 dynamic extensometer with a 12.5 mm gauge length and ± 5 mm strain. The average measured values and standard deviation for the three specimens are a modulus of elasticity of 168 ± 4 GPa, a tensile strength of 637 ± 4 MPa, a yield strength of 502 ± 8 MPa, and a longitudinal elongation of $35.4 \pm 3.0\%$.

2.2. Fatigue tests conditions

The experimental test programme determines the effect of specimen length on the failure probability for the fatigue strength distribution of the PBF-LB 316L steel. The range of the controlled stress state in the specimen is based on uniaxial high-cycle fatigue testing. The fatigue tests are carried out in accordance with ISO 1099 [26] and ISO 12107 [27]. A sinusoidal tensile loading ($R = 0.01$) was applied to prevent buckling of low stiffness specimens. For the assumed frequency of 20 Hz, there was no significant increase in the specimen temperature. The final criterion for the fatigue test was a continuous crack, in the plane normal to the load axis. The fatigue tests were carried out on the same machine as the static tensile test. The identified parameters were used as constants in the test programme. The statistical size effect studies require minimising the influence of other factors that significantly affect the output of the experimental tests.

Fig. 4 shows the geometry of smooth specimens, varying in the length of the working part. The defined variable l_w was used as an input parameter to the test programme. The method of dimension change determines non-proportional scaling. Table 1 shows the dimensions of the specimen geometries. The machining was identical to the static tensile test specimens. The theoretical stress concentration factor (K_t) is constant for the selected group of specimens (L05, L20, L50). For specimen L00, the K_t factor is equal to 1.08. The dimensional relationships used have a negligible effect on the result. Therefore, the data have not been corrected. The specimens were tested to a maximum cyclic normal stress (S_{max}) of 450 MPa. The applied load determined a fatigue life not greater than the number of cycles for the assumed knee point of the fatigue curve ($5 \cdot 10^5$ cycles [28]). The output of the test programme was the fatigue life for the selected stress level.
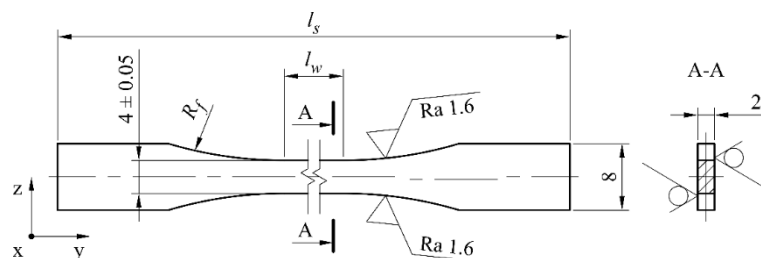

Fig. 4. Geometry of the unnotched stress controlled fatigue test specimens made of the PBF-LB 316L stainless steel.

Table 1. Specimen dimensions for variable length.

Specimen number	Dimension [mm]			Number of specimens, n
	l_w	l_s	R_f	
L00	0	35	12	10
L05	5	60	50	10
L20	20	80	50	10
L50	50	110	50	10

3. Results and discussion

3.1. High-cycle fatigue

The fatigue failure process is a non-deterministic phenomenon, usually described by a probabilistic model based on a Weibull distribution. The resulting failure probability represents the relationship between the stress level of a fatigue cycle and the number of cycles to failure. The parameters of the Weibull distribution are estimated using the maximum likelihood method. The cumulative failure probability can be determined using a three-parameter Weibull distribution, according to the equation [6]:

$$P_f\left(N_f, S_f\right) = 1 - \exp\left[-\left(\frac{(N_f, S_f) - \lambda}{\delta}\right)^{\alpha}\right] \tag{1}$$

where N_f is the number of cycles to failure, S_f is the fatigue strength, α is the shape parameter, δ is the scale parameter, λ is the location parameter.

Fig. 5 shows experimental results for selected failure probabilities. The diameter of the points determines the measured size of the critical defect. The parameter $\sqrt{area}$ is defined as the square root of the defect area projected onto a plane perpendicular to the applied maximum principal stress. The detailed data are presented in Sections 3.2, 3.3. The solid line is the cumulative distribution function (CDF) for the variable failure probability (P_f). The location of the vertical dashed lines for P_f of 50% shows a decrease in fatigue life with increasing specimen length. The observed size effect significantly affects the results. The defect size correlates with the fatigue properties. An increase in defect size decreases fatigue life.

A useful engineering design approach is the implementation of fatigue strength based calculation methods. The implemented procedure uses a constant linear regression slope coefficient (m_{exp}) of the experimental fatigue curve for a fully reversed cycle. The fatigue tests for a R ratio of -1 were carried out on a high stiffness specimen (L00). Fig. 6 shows the results for a variable R ratio. A regression model for P_f of 50% (solid line) was used to estimate the fatigue strength ($S_{f,est}$) for variable length specimens. The coefficient b_{est} was calculated using the experimental fatigue life ($R = 0.01$), a constant stress level (S_{max}) and a coefficient m_{exp} ($R = -1$). The fatigue strength ($S_{f,est}$) was estimated for $5 \cdot 10^5$ cycles and coefficients m_{exp}, b_{est}. The output as a function of the failure probability is considered for further analysis.
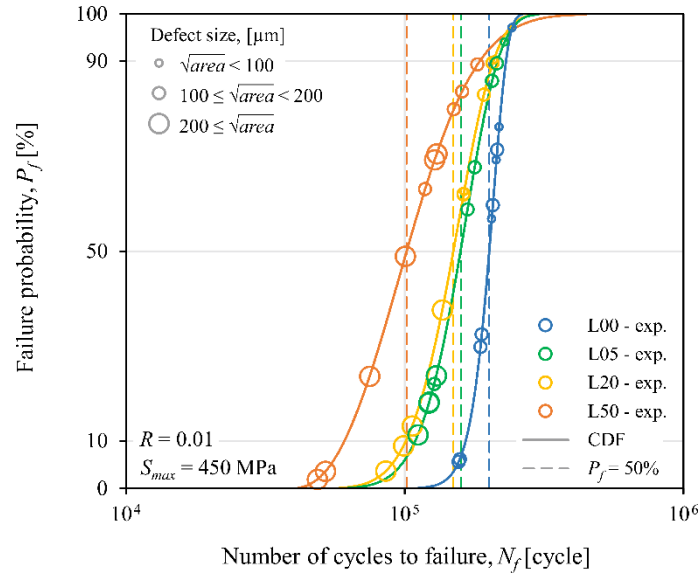
Fig. 5. Cumulative Weibull distribution function for experimental data of variable length specimens.
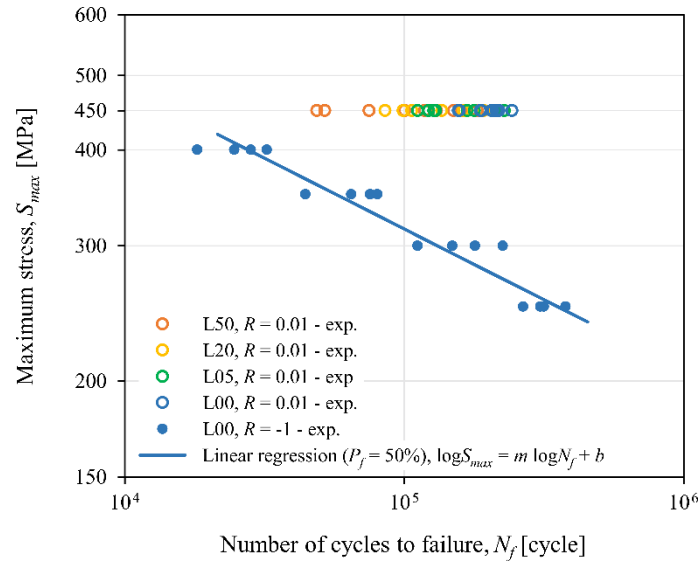

Fig. 6. Experimental high-cycle fatigue data for variable R ratio.

Table 2. Results of Weibull distribution for experimental fatigue life ($R = 0.01$) and estimated fatigue strength range ($R = -1$).

Specimen number	Weibull distribution ($\log N_f$)			P_f [%]	N_f [cycle] $S_{max} = 450$ MPa, $R = 0.01$	$\Delta S_{f,est}$ [MPa], $R = -1$
	λ	α	δ			
L00	4.84	9.67	0.48	10	166 085	453
				50	200 582	469
				90	230 938	481
L05	4.75	4.53	0.49	10	110 512	420
				50	157 554	448
				90	216 163	475
L20	4.72	4.14	0.49	10	101 164	413
				50	147 791	443
				90	209 478	472
L50	4.59	2.47	0.49	10	60 852	376
				50	101 843	415
				90	186 380	462

Table 2 shows the parameters of the Weibull distribution Eq. (1) for the logarithmic number of cycles to failure. The shape parameter (α) increases as the specimen length decreases. The correlation determines the decrease in fatigue strength scatter for the smaller specimen. The location parameter (λ) follows the trend of fatigue properties as a function of specimen size. The behaviour of the material is consistent with theoretical assumptions [21]. The relationship between the size effect and the failure probability is observed. An increase in the P_f variable correlates with a decrease in the size effect on the fatigue properties of the PBF-LB 316L steel.

3.2. Crack initiation

The fractographic analysis was used to assess the failure mechanism of the PBF-LB 316L steel. The specimens were observed using a JEOL 6480LV scanning electron microscope in the secondary electron mode with an accelerating voltage of 20kV. Fig. 7 and Fig. 8 show examples of fracture surfaces in a plane perpendicular to the y-axis loading direction. The views are defined on the same scale. All cracks initiated from a one site. The specimens L05, L20, L50 failed at the smallest width. A critical defect, defined as a defect on the fracture surface that initiates the main crack, was identified for each specimen. The boundary between the defect and the fracture surface is marked by a closed curve (dashed line). The defect size ($\sqrt{area}$) was measured using image analysis software. The observed defects are characterised by a deep area, resulting from a lack of fusion of subsequent material layers, containing multiple unmelted powder grains and pool inhomogeneities (Fig. 7a-d). The process of defect formation determines the inaccuracy of additive manufacturing, according to the microstructure analysis (Section 2.1). The initiation site was identified by characteristic river pattern on the flat transgranular crack plane. The smaller defects located on the fracture surface joined the main crack propagation path. For the smallest specimens, a few flat areas of crack initiation were observed due to microstructural effects of the steel matrix (Fig. 7e), caused by cyclic plastic strain.

The measured defect sizes correlate with the fatigue properties of the PBF-LB 316L steel. An increase in the parameter $\sqrt{area}$ determines a decrease in fatigue life. Fig. 7a shows the largest critical defect detected in the experimental data population. Subsequent views show selected defects located in the subsurface volume. All cracks were initiated in the surface region after machining. The variable width to length ratios of the defects do not suggest a significant effect on fatigue life. Two types of defects were observed, surface (Fig. 7) and subsurface (Fig. 8). A subsurface defect defines the lack of connection between the defect boundary (dashed line) and the outer surface of the specimen. Belonging to a defined defect type determines the implementation of the statistical size effect model described in Section 3.4.2. The crack initiation observed is a common failure mechanism in additively manufactured materials [29-34].

The analysis of defects in the material structure (Fig. 3) identified the location of large internal pores at a significant distance from the outer surface (over 200 µm). An assessment of the fracture surface does not reveal any such defects. All detected fatigue crack initiating defects are located in the subsurface volume. These defects determine higher cyclic plastic strains than the internal defect, while speeding up the crack initiation [35]. A subsurface defect increases the failure probability than an internal defect because it has a smaller propagation area towards the open surface [36]. An internal crack growing in a vacuum determines a lower propagation rate than a surface crack [37], as confirmed by the non-detection failure for a high applied stress level [38]. A surface defect close to the surface shows faster crack initiation than a surface defect [21]. The applied uniaxial cyclic loading generates a multiaxial stress state in the bridge zone of the material between the defect and the outer surface [39]. A small subsurface defect may be more critical than a surface defect. The location of critical defects is consistent with a highly stressed volume of $90\%\sigma_{max}$ (Section 3.4.1).

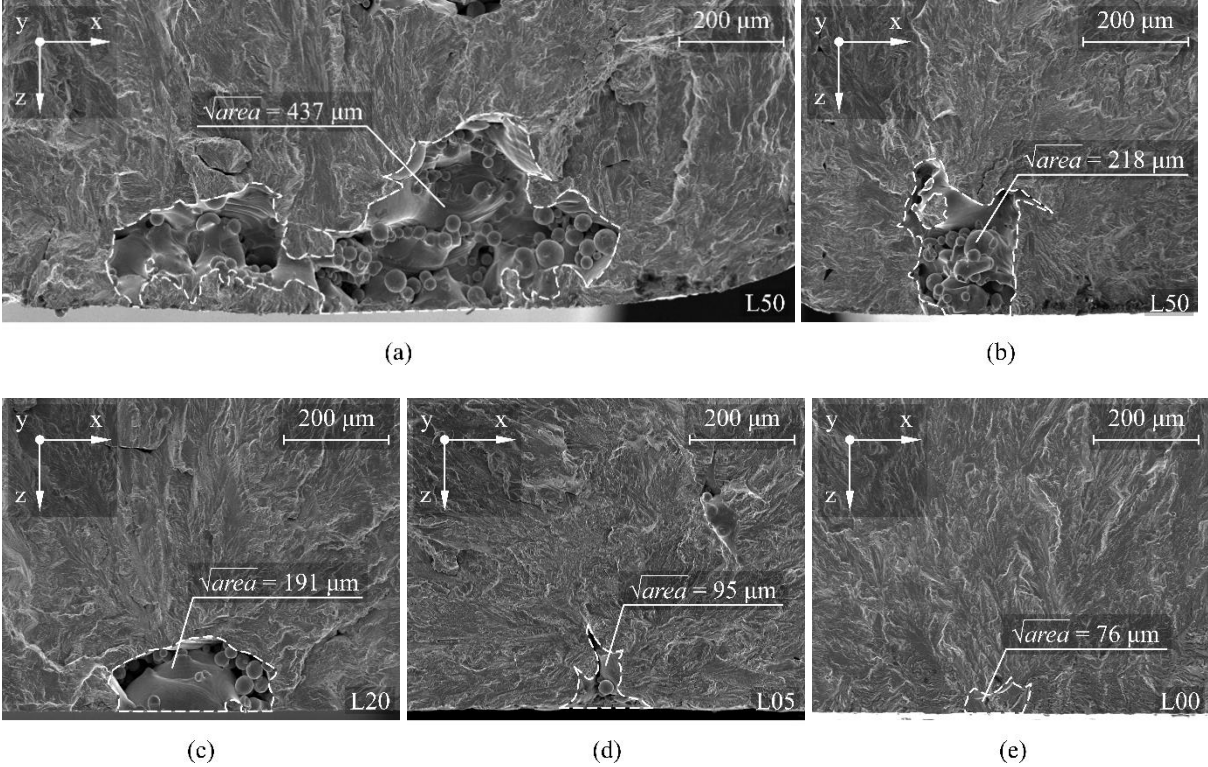

Fig. 7. Fracture surface in the area of the surface critical defect initiating the fatigue crack, specimen: a) L50_02 – N_f = 51 895, b) L50_07 – N_f = 130 283, c) L20_06 – N_f = 162 698, d) L05_10 – N_f = 227 987, e) L00_07 – N_f = 213 306.
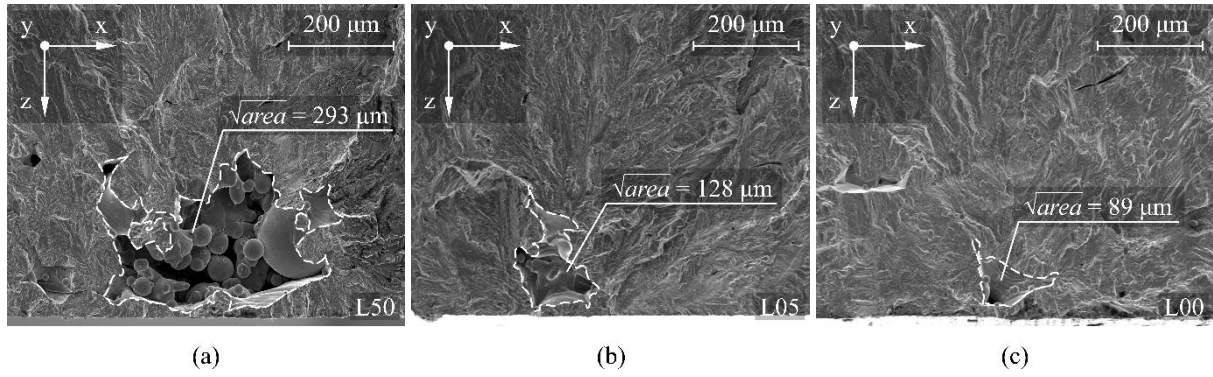
Fig. 8. Fracture surface in the area of the subsurface critical defect initiating the fatigue crack, specimen: a) L50_03 – N_f = 74 804, b) L05_08 – N_f = 205 835, c) L00_09 – N_f = 218 167.

3.3. Defect size

The analyses assume that the size and location of a single defect are the main variables controlling the failure of the PBF-LB 316L steel. This random variable is described by a log-normal distribution. The parameter $\sqrt{area}$ was determined for the marked defect boundary shown in Fig. 7 and Fig. 8. The range of values obtained for all specimens is from 53 μm to 437 μm. Table 3 shows all the data. Fig. 9 shows the measured sizes of surface defects (solid points) and subsurface defects (empty points). The parameter $\sqrt{area}$ is related to the specimen length (l_w). The solid line corresponds to the mean value. The data increases non-linearly with the defined size.

Table 3. Compilation of experimental and estimated data for the PBF-LB 316L stainless steel.

Specimen number	N_f [cycle], S_{max} = 450 MPa, R = 0.01	$\Delta S_{f,est}$ [MPa], R = -1	$\sqrt{area}$ [μm]	Defect type	Form of defect
L50_01	48 587	413	397	surface	void
L50_02	51 895	433	437	surface	void
L50_03	74 804	461	293	subsurface	void
L50_04	100 384	432	312	subsurface	void
L50_05	118 304	450	188	surface	void
L50_06	128 028	361	224	subsurface	void
L50_07	130 283	444	218	surface	void
L50_08	150 080	391	139	surface	matrix
L50_09	160 603	425	125	surface	void
L50_10	182 324	365	103	surface	void
L20_01	85 375	400	268	subsurface	void
L20_02	98 988	465	352	surface	void
L20_03	106 289	451	230	surface	void
L20_04	136 345	472	205	surface	void
L20_05	162 545	471	173	subsurface	void
L20_06	162 698	451	191	surface	void
L20_07	163 218	451	99	surface	matrix
L20_08	192 180	437	173	subsurface	void
L20_09	206 834	412	106	surface	void
L20_10	208 462	417	99	surface	void
L05_01	111 462	431	205	surface	void
L05_02	122 051	474	251	surface	void
L05_03	122 316	471	225	surface	void
L05_04	127 479	480	195	surface	void

| L05_05	129 658	428	211	subsurface	void
L05_06	167 975	454	170	surface	void
L05_07	178 235	428	175	subsurface	void
L05_08	205 835	459	128	subsurface	void
L05_09	214 122	433	104	surface	void
L05_10	227 987	421	95	surface	void
L00_01	156 105	448	191	subsurface	void
L00_02	157 495	474	134	surface	void
L00_03	186 934	486	168	surface	void
L00_04	189 007	471	112	surface	void
L00_05	205 305	448	69	surface	void
L00_06	207 146	464	159	subsurface	void
L00_07	213 306	476	76	surface	matrix
L00_08	214 797	475	101	subsurface	void
L00_09	218 167	463	89	subsurface	void
L00_10	242 983	472	53	surface	matrix
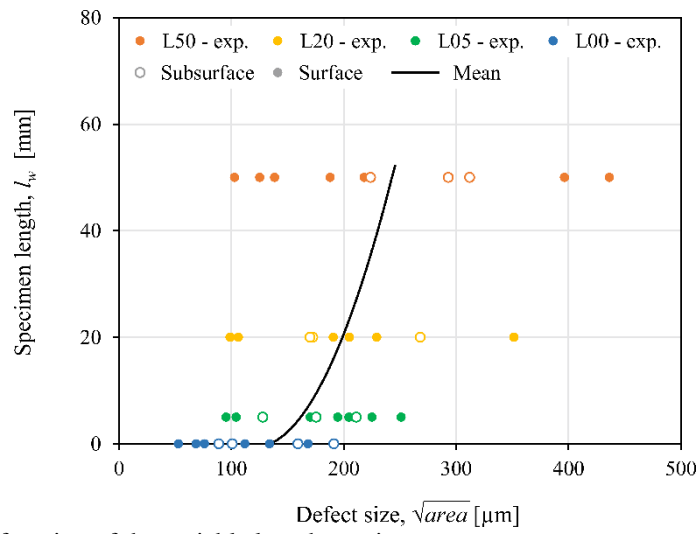
Fig. 9. Defect size as a function of the variable length specimen.

The defect size that determines fatigue strength is the critical defect initiating failure in a uniform cyclic stress field. The correlation between fatigue strength and critical defect size is shown in the Kitagawa-Takahashi diagram [40]. The original form defines the relationship between the "fatigue limit" and the propagating fracture state according to linear elastic fracture mechanics. A practical use of the diagram for materials with defects requires the crack length to be replaced by the parameter $\sqrt{area}$. The results of analyses consistent with this approach are presented in the papers [41-45]. The diagram was plotted for the range of estimated fatigue strength ($\Delta S_{f,est}$), calculated from the experimental fatigue life (N_f) for a constant level of cyclic maximum stress.

The correlation between defect size and fatigue strength is defined by the empirical Murakami criterion. The approach uses $\sqrt{area}$ as the geometric parameter and Vickers hardness as the material parameter. The fatigue strength for varying mean stress is determined from the equation [21]:

$$S_f(\sqrt{area}, HV, R) = \frac{d_l\,(HV + 120)}{\sqrt{area}^{1/6}}\left(\frac{1-R}{2}\right)^{\alpha_M} \tag{2}$$

$$\alpha_M(HV) = 0{,}226 + HV \cdot 10^{-4} \tag{3}$$

where d_l is the defect type (surface defect – 1,43; subsurface defect – 1.41), R is the stress ratio and HV is the Vickers hardness. Below the threshold fatigue strength calculated from the equation, the failure does not occur. The initiated crack does not propagate to a critical size. The defect is treated as a crack correlating with fatigue strength. If the defect is smaller than the critical size then the fatigue strength depends on the microstructural properties defined by hardness.

The implementation of Eq. (2) is valid for the experimentally determined upper limit, below which the decrease in fatigue strength is noticeable. The occurrence of a plateau is determined by the characteristics of the material structure, including the ability to propagate microcrack through microstructural barriers to macrocrack. The full range of the crack initiating defect size is described by the El-Haddad model [46], which assumes a smooth transition from a short to a long crack. In the original form of the equation, a fictitious crack length was implemented. This constant for materials with defects corresponds to the parameter $\sqrt{area}_0$. The region below this value represents the range of long crack propagation based on linear elastic fracture mechanics. The modified El-Haddad model takes the form:

$$\Delta S_f(\sqrt{area}) = \Delta S_{f,0} \sqrt{\frac{\sqrt{area}_0}{\sqrt{area}_0 + \sqrt{area}}} \tag{4}$$

where $\sqrt{area}_0$ is the material constant of the Murakami parameter, $\Delta S_{f,0}$ is the upper limit of fatigue strength range.

The approximation of the experimental data using the Murakami model, Eq. (2) and El-Haddad, Eq. (4) in its original form provides a deterministic result. A proposed modification to the selected approaches is the definition of a probabilistic measure. The input parameters of the models that best fit the data were obtained by the least squares method. The variation of fatigue strength was described by a probabilistic model using a three-parameter Weibull distribution function. Fig. 10a shows the distribution for the normalized fatigue strength range calculated from the ratio of the data estimated from Eqs. (2), (4) and the mean. The points show the confidence interval (α_0 = 0.05). The variation in the location of these limits is noticeable.

The prediction results of the Murakami model were obtained for all input data and defects above the assumed size. The analysis was carried out to determine the critical defect size limit that significantly affects the fatigue strength decrease. A good fit was obtained for data above a parameter $\sqrt{area}$ of 100 µm. The coefficient of determination (R^2) increased from 0.693 to 0.812 after removing the data below this limit. The defect size below this value disturbs the linearity of the model and significantly increases the confidence interval limits of the Weibull distribution. The exclusion of defects below a defined size determines the process of fatigue crack

initiation and propagation. An attempt to explain this phenomenon is provided by the theory of critical distance [47, 48]. The failure is determined by exceeding the average stress in the volume around the peak value generated by the defect. A small defect of less than 100 µm generates a large local stress gradient and low average stress in a defined volume. The local stress state does not speed up fatigue crack initiation. The process is determined by the microstructural characteristics of the material.

Fig. 10b and c show the estimation results of the analysed models for variable specimen length. Each point is the defect size in relation to the estimated fatigue strength range ($\Delta S_{f,est}$) using a regression model with a R ratio of -1 and $5 \cdot 10^5$ cycles (Table 3). The material shows sensitivity of fatigue properties as a function of defect size. The dashed lines represent the confidence interval limits ($\alpha_0 = 0.05$). The defect size above the lower limit determines the fatigue failure. The Murakami model with a 1:6 slope of lines was limited in the upper fatigue strength (for the mean – 482 MPa). The coefficient d_l depending on the defect type (surface, subsurface) was considered. The El-Haddad model shows asymptotic behaviour for $\Delta S_{f,0}$ (for the mean – 517 MPa). All measured defect sizes are below the threshold value $\sqrt{area}_0$ of 486 µm. Fig. 10d shows selected log-normal distributions of defect size for specimens L00, L50. The points are the measured defect sizes in the defined specimen population. The vertical dashed line shows the defect size calculated for 50% probability (mean), 107 µm and 219 µm, for specimens L00 and L50, respectively. The location of the log-normal distributions indicates an increase in defect size with specimen length.

Table 4 summarises the approximation results of the models. A higher coefficient of determination (R^2) points a better fit of the data estimated for the El-Haddad model. The Weibull distributions show a similar correlation, with a higher shape parameter (α) defining a lower data scatter. The observed scatter is a microstructural effect that determines fatigue crack initiation and propagation, a combination of the size, the defect localisation, the local residual stresses and the anisotropy of the material properties. The predicted fatigue strength ($\Delta S_{f,pred}$) for failure probabilities (P_f) of 10%, 50%, 90% was calculated using the log-normal distribution of the actual defect size for the selected specimen size (Fig. 10d). The relative error (δ_p) was calculated in relation to the experimental data in Table 2. The mean absolute percentage error for both models is similar at 1.4%. The implementation of models at the engineering design stage is unsafe. Both approaches overestimate the predicted data for the longest L50 specimen. The relationship between fatigue strength and object size can be related to a measure of material failure using the statistical distribution of $\sqrt{area}$. The size effect of the material with defects can be modelled for a defined correlation of these variables using extreme value statistics.
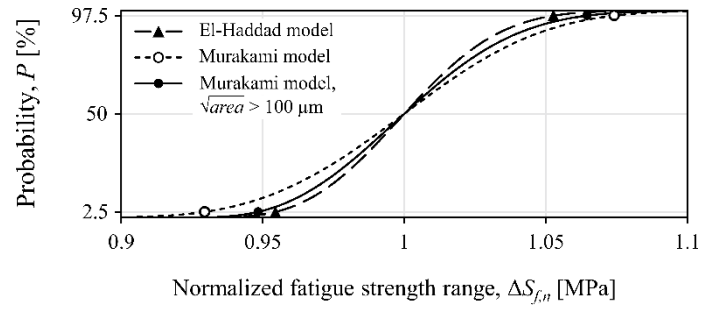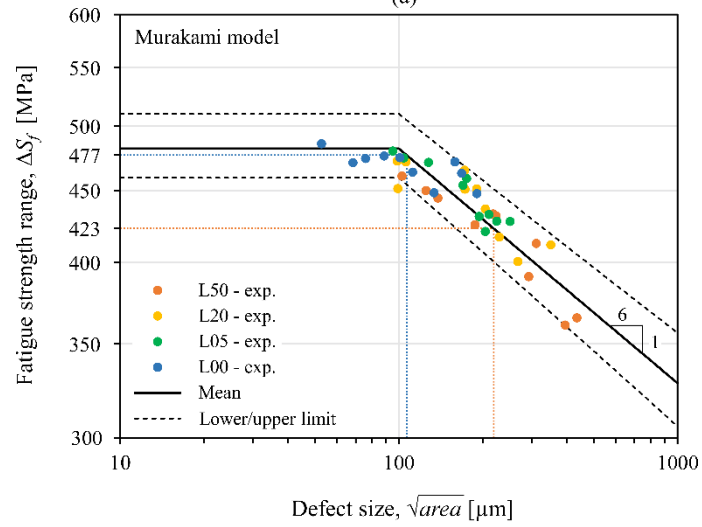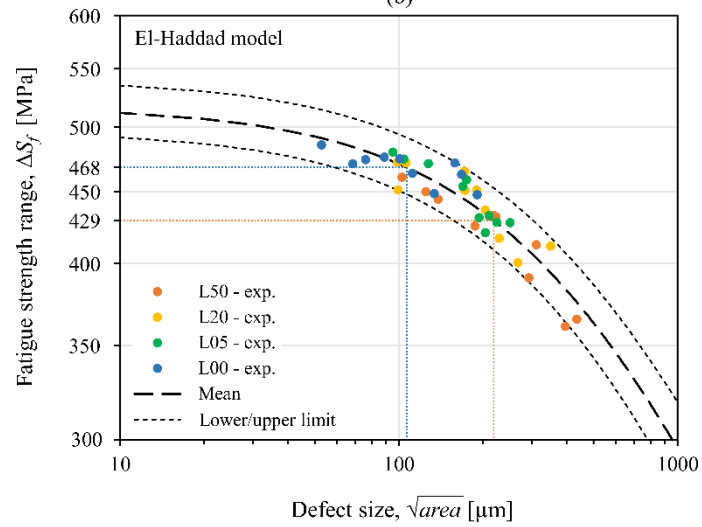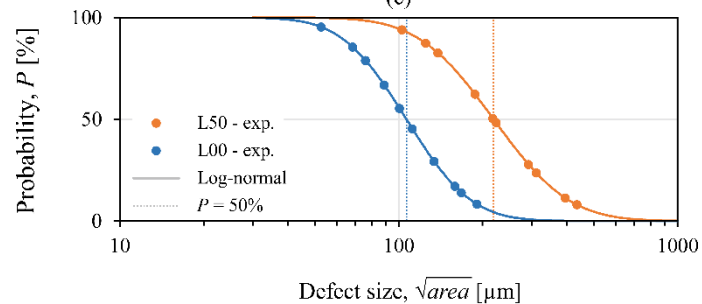
Fig. 10. Effect of critical defect on fatigue strength for a *R* ratio of -1 and $5 \cdot 10^5$ cycles: a) Weibull distributions for estimated data, b) Murakami model, c) El-Haddad model, d) log-normal distributions for defect size.

Table 4. Fatigue strength prediction results using Murakami, El-Haddad model and defect size distribution for varying failure probability and specimen length.

Model	Parameters for mean	R^2	Weibull dist. ($\Delta S_{f,n}$)			$\Delta S_{f,pred}$ [MPa] (δ_p [%])				
			λ	α	δ	P_f [%]	L00	L05	L20	L50
Murakami, $\sqrt{area} \geq 100$ µm, Eq. (2)	$HV = 243$	0.812	0.93	2.61	35.9	10	436 (-3.7)	411 (-1.9)	412 (-0.2)	381 (1.2)
						50	477 (1.7)	439 (-2.2)	442 (-0.3)	423 (2.0)
						90	482 (0.1)	468 (-1.6)	475 (0.5)	469 (1.7)
El-Haddad, Eq. (4)	$\sqrt{area}_0 = 486$ µm $\Delta S_{f,0} = 517$ MPa	0.849	0.93	2.85	33.4	10	441 (-2.7)	418 (-0.4)	419 (1.3)	381 (1.1)
						50	468 (-0.2)	443 (-1.2)	446 (0.6)	429 (3.5)
						90	487 (1.2)	463 (-2.6)	467 (-1.1)	464 (0.6)

3.4. Procedure for predicting size effect

The prediction of the size effect on fatigue behaviour was implemented using a statistical approach. The probability of a defect decreasing the fatigue strength increases with material volume. Fig. 11 shows the modelling steps of the proposed procedure. The dashed areas indicate the input data. The size ($\sqrt{area}$) and location (t_b) parameters define the defect. Both variables are probabilistic measures, described by a distribution of random values. The defect location is identified by the highly stressed volume ($V_{n\%}$). The number of defects (n_d) is the result of the highly stressed volume and the defect density (ρ_d). The simulation of random defect distributions are generated depending on the parameters ($V_{n\%}$, $\sqrt{area}$, t_b, ρ_d) for the selected population of numerical specimens until the n_d variable is reached. The defect criticality defines the fatigue criterion for the nonlocal stress distribution in the defect. A population of critical defects is generated until the number of specimens (n) is reached. The fatigue strength ($S_{f,pred}$) described by a probabilistic scatter band is predicted from the extreme value statistics and the model describing the Kitagawa-Takahashi diagram. The implementation of this procedure for the selected variables provides output for an object of any size.
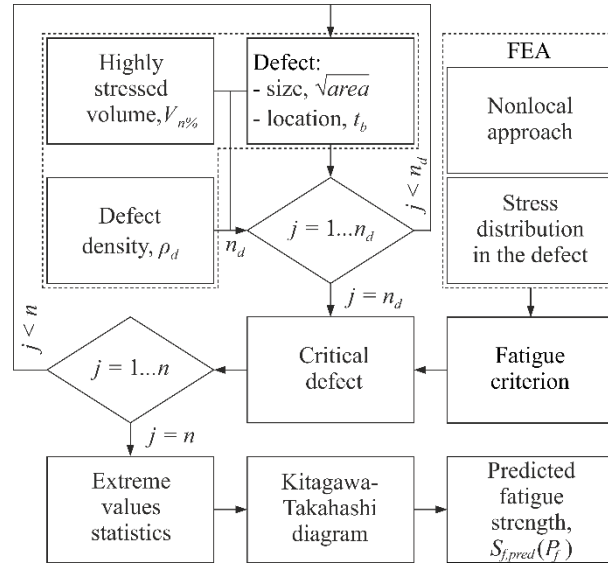
Fig. 11. Schematic of the fatigue strength prediction procedure for a variable size object with material defects.

3.4.1. Simulation of defect distribution

The random defect generation procedure has been implemented for a numerical model with defined variables. Similar methods for modelling the defect distribution are reported in the papers [49, 50]. The analysed method locates the defect in a highly stressed volume (HSV). The size of the HSV was calculated numerically using the finite element method (FEA) with ANSYS software. The analyses have been carried out in the structural analysis module with fixed boundary conditions. The material is an isotropic linear elastic model. The CAD model geometry was identical to the fatigue specimen (Fig. 4, Table 1). The solid elements with 20 nodes and three degrees of freedom per node (SOLID186) were used. The results of the discretisation error analysis determined the size of the finite element mesh. Fig. 12a shows an example of a normal stress distribution map along the y-axis for specimen L05. The scale determines the $n\%$ parameter for HSV. A tensile loading F was applied to the top and bottom surfaces in the y-axis direction.

Fig. 12b shows a visualisation of the defect distribution in HSV for $n\%$ of 90%. The value was determined empirically, according to the paper [39]. A parametric CAD model was created using a specially provided macro. The defects are represented as idealised, simplified spherical objects. Each defect was given a colour corresponding to the selected $\sqrt{area}$ range according to the scale. The Monte Carlo method and the Mersenne Twister algorithm are used to generate the numerical specimens. The simulated defect location is determined by random values within the HSV limits. A random defect size is related to the generated location coordinates. The procedure is repeated until the number of defects (n_d) is reached, according to the procedure scheme (Fig. 11). The model can be created for any defect distribution and specimen size. The modelling of all defects in a finite volume provides an assessment relative to other defects. Based on the fracture surface results in Section 3.2, the analysis is simplified

to a single critical defect. The method was used to generate the numerical data described in Section 3.5. The critical defect identified is the correlation between the maximum defect size and the minimum distance from the outer surface of the specimen. A detailed analysis is presented in Section 3.4.2.
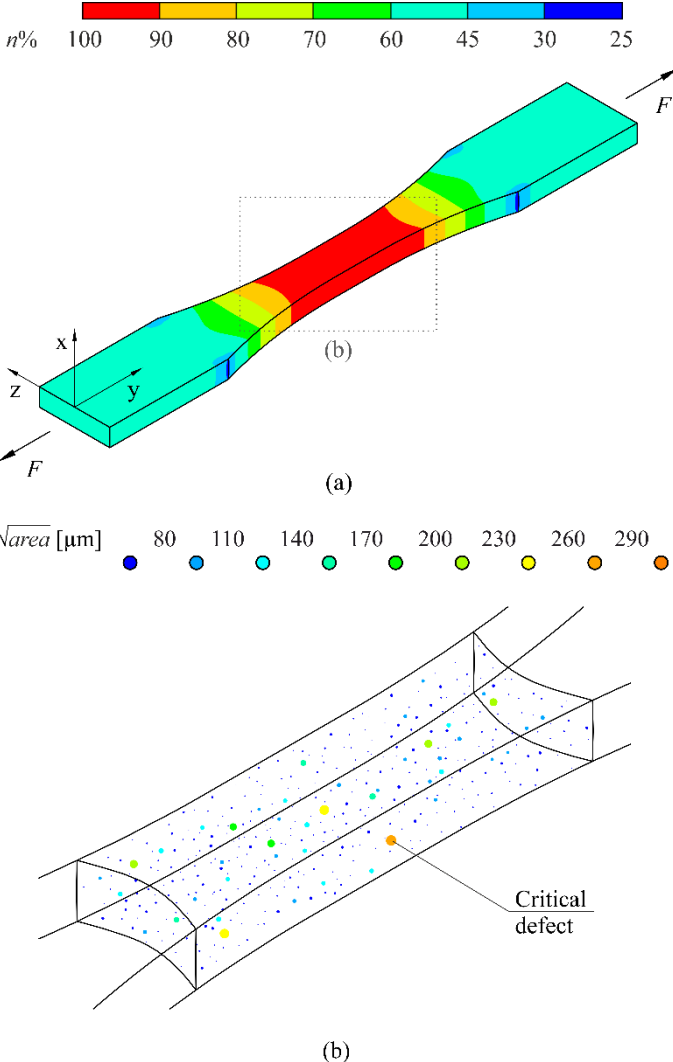

Fig. 12. Visualization of defect distribution in highly stressed volume (L05): a) normal stress distribution map along the y-axis, b) example of defect distribution at $V_{90\%}$ for a density ρ_d of 0.1%.

The number of defects (n_d) in a limited volume of material is determined by the defect density (ρ_d) as the ratio of the defect volume to the highly stressed volume for $n\%$. The analyses were carried out for an assumed value of 0.1%. A random defect size ($\sqrt{area}$), following a log-normal distribution, is prescribed for the three-dimensional defect location. The defect location is determined by the random defect distance (t_b) from the outer surface of the specimen. The defects are located in a subsurface volume of thickness t_d according to the fractographic analysis in Section 3.2. This parameter is defined as the maximum distance of the extreme critical defect point from the outer surface of the object. The dimension t_d is a material constant, independent of the specimen size. Table 5 summarises

the numerically calculated HSV for each specimen size, including the constant t_d. This data was used for further analysis.

Table 5. Numerical value of highly stressed volume 90% σ_{max} for variable specimen length (t_d = const.).

Specimen number	L00	L05	L20	L50
$V_{90\%}$ [mm^3]	7.9	63.5	138.5	288.5

3.4.2. Defect criticality

A quantitative measure of defect criticality is the equivalent stress, calculated using the Crossland multiaxial fatigue criterion [51] and analysed in other papers [52-54]. The criterion determines the effect of cyclic stress on fatigue failure, without defining the crack orientation [55]. The equation is shown below:

$$\sigma_{CR} = \sqrt{J_{2,a}} + \alpha_{CR} J_{1,max} \leq \beta_{CR} \tag{5}$$

where $J_{2,a}$ is the amplitude of the second invariant of a deviatoric stress tensor, $J_{1,max}$ is the maximum hydrostatic stress, α_{CR} and β_{CR} are the material constants according to the equations:

$$\alpha_{CR} = \frac{3\tau_w}{\sigma_w} - \sqrt{3} \tag{6}$$

$$\beta_{CR} = \tau_w \tag{7}$$

where σ_w is the fatigue strength at a knee point of fully reversed tension/compression, τ_w is the fatigue strength at a knee point of fully reversed torsion. The value of $J_{2,a}$ is determined by double maximisation over the loading cycle. The ratio of the Crossland stress (σ_{CR}) to the threshold parameter β_{CR} defines the normalized equivalent stress ($\sigma_{CR,n}$).

The sensitivity of the fatigue strength to defect location relative to the outer surface (t_b) and the defect size ($\sqrt{area}$) is estimated by a quadratic surface regression equation, as follows [39]:

$$\sigma_{CR,n} = \beta_0 + \beta_1\sqrt{area} + \beta_2 t_b + \beta_3\sqrt{area}\,t_b + \beta_4\sqrt{area}^2 + \beta_5 t_b^2 \tag{8}$$

where β_0 is the intercept, $\beta_1 - \beta_5$ are the regression coefficients (1-α_0 = 0.95). An extension of the concept of the Murakami model Eq. (2), instead of the defect type (d_l), is the consideration of the defect location distance. The determination of the parameters in Eq. (8) required finite element analysis of representative element volume (RVE) modelling for the defined variables. The results showed an increase in the stress distribution components of the Crossland criterion for selected combinations of t_b and $\sqrt{area}$. The macroscopic stress gradient around the defect was considered by implementing a nonlocal method for a defined sphere. The details are provided in the paper [39]. Table 6 summarises the data for the second-order model. The analytical calculation of the stress $\sigma_{CR,n}$ significantly reduces the time required compared to FEA. For the generated defect population in the numerical specimen, as shown in Fig. 12b, the criticality for each defect is calculated using Eq. (8). The proposed material

definition depends on the defect parameters, the defect density and the size of the highly stressed volume, according to the procedure scheme (Fig. 11).

Table 6. Coefficients of analytical model for output variable $\sigma_{CR,n}$ [39].

Defect	β_0	β_1	β_2	β_3	β_4	β_5
Surface	0.7962	0.0018	-	-	-	-
Subsurface	0.8314	0.0026	-0.0054	$-4.6664 \cdot 10^{-6}$	$5.57 \cdot 10^{-8}$	$3.4855 \cdot 10^{-5}$

### 3.4.3. Verification of fatigue criterion

The consideration of the stress state around the defect using the Crossland criterion has been implemented for two parameter combinations (Eq. (8)). Fig. 13a shows the Weibull distribution for the normalized fatigue strength range. The defect type was analysed as surface only (dashed line) and according to the actual location of the defect (solid line). The points defining the confidence interval ($\alpha_0 = 0.05$) indicate a significant difference in location.

Fig. 13b shows the results of the linear regression model for the normalized Crossland stress and the estimated fatigue strength range ($\Delta S_{f,est}$) using a regression model with a R ratio of -1 and $5 \cdot 10^5$ cycles (Table 3). The points identify the actual defect location, which is important for the implementation of the analytical model (Eq. (8)). Most of the cracks were initiated by surface defects (solid points). The crack initiation from the matrix is a small percentage in relation to the voids and does not significantly affect the result. The model output is provided for defects above the parameter $\sqrt{area}$ of 100 µm ($\sigma_{CR,n} > 1$). The coefficient of determination (R^2) increased from 0.867 to 0.904 after accounting for subsurface defects. In this population of experimental data, the consideration of subsurface defects significantly affects the model fit. Fig. 13c shows selected log-normal distributions of normalized Crossland stress for specimens L00 and L50. The points were calculated for the actual defect parameters using Eq. (8). For a 50% probability (mean), a stress of 1 and 1.24 was obtained for specimens L00 and L50 respectively. The result for specimen L00 suggests the limits of the size effect on fatigue properties. Below this size, the effect of defects should be minor.

Table 7 shows the results of the linear regression approximation for the normalized Crossland stress. The model input parameters calculated by the least squares method give a better fit to the output data than the Murakami model and the El-Haddad model. The R^2 coefficient is higher. The predicted results have smaller relative errors (δ_p). The mean absolute percentage error is at 1.0%. An attempt to capture selected combinations of defect variables using the proposed calculation procedure is justified. An extension of the commonly used procedures for parameter $\sqrt{area}$ could be to implement a failure measure definition using a nonlocal stress around the defect, taking into account the size and location of the defect.
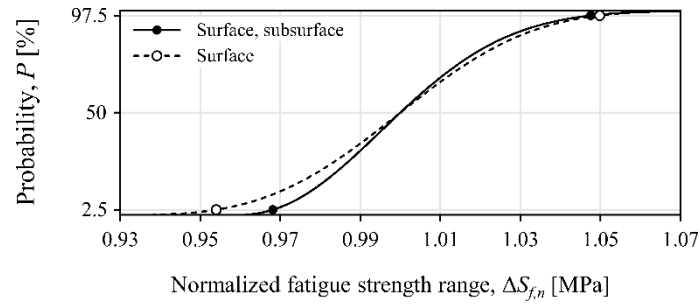
(a)
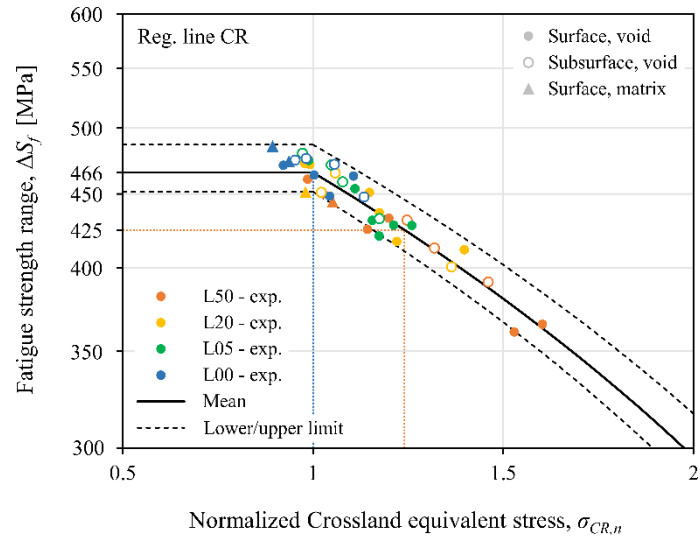
(b)
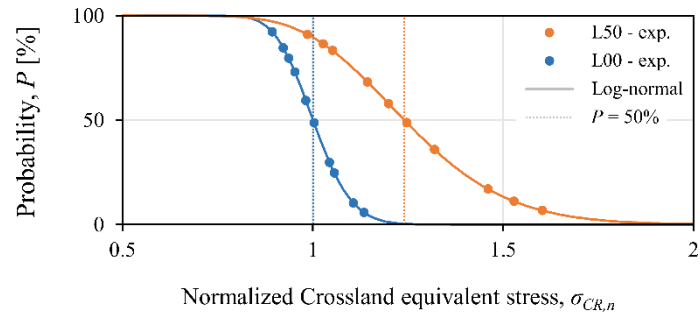
(c)

Fig. 13. Effect of critical defect on fatigue strength using Crossland criterion for a R ratio of -1 and $5 \cdot 10^5$ cycles: a) Weibull distributions for estimated data, b) linear model for normalized stress, c) log-normal distributions for normalized Crossland equivalent stress.

Table 7. Fatigue strength prediction results using linear model for normalized stress and defect size distribution for varying failure probability and specimen length.

Model	Parameters for mean	R^2	Weibull dist. ($\Delta S_{f,n}$)			$\Delta S_{f,pred}$ [MPa] (δ_p [%])				
			λ	α	δ	P_f [%]	L00	L05	L20	L50
Reg. line CR $\Delta S_f = m\, \sigma_{CR,n} + b$	$m = -169.9$ $b = 635.6$	0.904	0.93	2.15	21.3	10	447 (-1.2)	424 (1.1)	409 (-1.1)	373 (-0.9)
						50	466 (-0.7)	446 (-0.5)	444 (0.2)	425 (2.4)
						90	482 (0.2)	466 (-1.9)	474 (0.5)	466 (1.0)

3.5. Verification of size effect model

The analyses of the correlation between fatigue strength and the critical defect size in the Kitagawa-Takahashi diagram (Section 3.3, 3.4.3) determine the data scatter of these two variables, described by the Weibull (Fig. 10a, Fig. 13a) and log-normal distributions (Fig. 10d), respectively. Fig. 14 shows the actual data scatter for the relationship between fatigue strength and failure probability. The location of the empty points on the abscissa axis is determined by the estimated fatigue strength using a data transfer procedure with a slope coefficient for fully reversed cycle results (Section 3). The values on the ordinate axis determine the predicted probability for the distribution of measured actual critical defect sizes for the selected specimen size (P for $\sqrt{area}$ – Fig. 10d). The combination of these two variables defines a significant data scatter with respect to the cumulative distribution function (solid line) of the estimated data. The size effect modelling assumes a probabilistic representation of these two variables (ΔS_f, $\sqrt{area}$). The data significantly determine the output to the parameter of the input distributions. Both probabilistic measures are material constants, independent of object size.
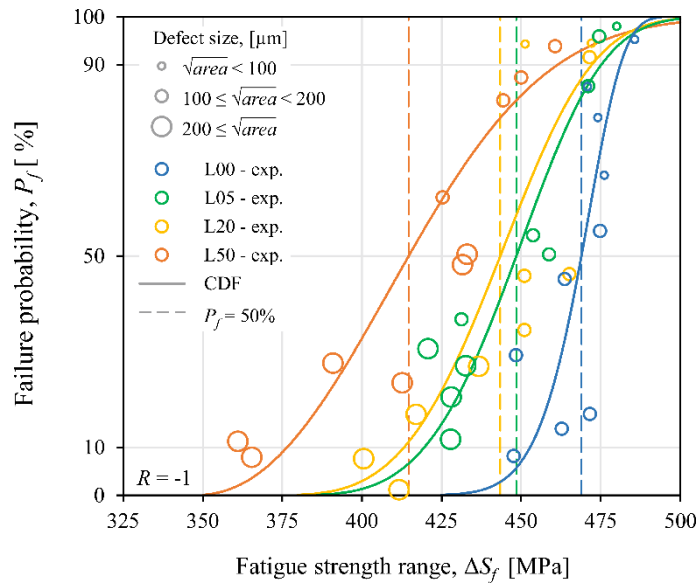

Fig. 14. Summary of estimated fatigue strength with experimental data scatter for variable length specimens.

The critical defect parameters were simulated for a variable size of a highly stressed volume. The procedure determines a random defect size ($\sqrt{area}$) following the input distribution and a random defect location (t_b). The algorithm for generating these parameters is repeated until the number of specimens (n) is reached, according to the procedure scheme (Fig. 11). Fig. 15 shows the simulated defect size distribution for reduced variance and probability. The defect size was indexed as $j = 1...n$, where it corresponding to the number of numerical specimens of 100. Each point is a defined critical defect in a numerical specimen. The values are ordered from smallest to largest, as shown below:

$$\sqrt{area}_1 \leq \sqrt{area}_2 \leq \cdots \leq \sqrt{area}_n \qquad\qquad\qquad\qquad\qquad\qquad (9)$$

The defect size was analysed using extreme value statistics [15, 56]. The solid line is the output log-normal distribution for the generated data (empty points). The results required the input of a highly stressed volume dependent on the specimen length (Table 5) and a constant defect density (ρ_d). The location variability of each distribution is consistent with the experimental data (solid points). The average defect size ($P = 50\%$) increases with the specimen size.
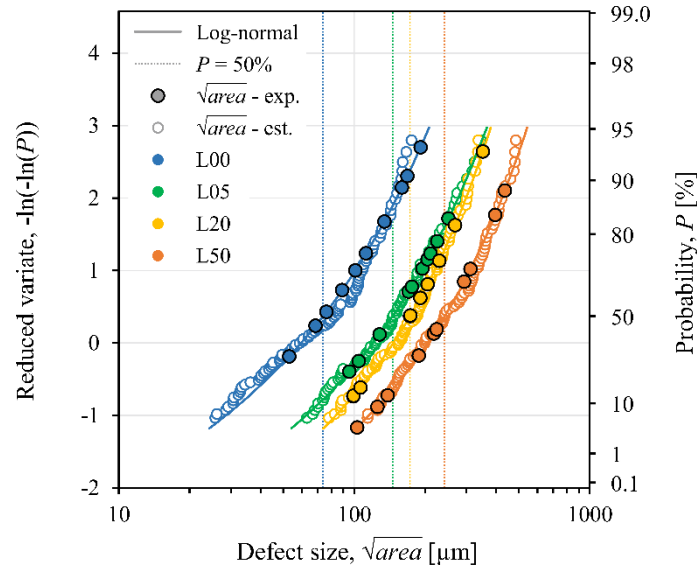

Fig. 15. Comparison of extreme value distributions for simulated critical defect size in variable size of highly stressed volume.

The second stage of probabilistic modelling determines the generation of random fatigue strength according to an estimated Weibull distribution. The input data are the results in Fig. 10a and Fig. 13a. For each critical defect (Fig. 15), the result was simulated using the Monte Carlo method within the confidence interval ($\alpha_0 = 0.05$) of the selected distribution. The output was calculated using the Murakami model ($\sqrt{area} > 100\mu$m), the El-Haddad model and the linear model for normalized stress. If the model allowed, the random defect location relative to the surface was considered.

The material constants were determined by implementing an iterative algorithm. The data were fitted with a maximum relative error of 0.5%. The condition was achieved at an average defect density of 0.1%. This procedure was carried out for the smallest specimen size (L00). The purpose of geometry selection is to take advantage of miniature specimen testing, including limited material volume [57, 58]. The input parameters were fitted using the Crossland stress normalized linear regression. The model selection is determined by the smallest implementation error, as described in Section 3.4.3. The similarity between the experimental and generated values is the result of fitting the input log-normal distribution ($\mu_0 = 2$, $\sigma_0 = 1.3$) to the output data.

Fig. 16 shows the simulation results for specimens L00 and L50. Due to the large number of variables, the results are presented for selected data. An identical calculation procedure was carried out for the other specimen sizes and the models. The dashed lines show the confidence interval of the input Weibull distribution. The distribution location (Fig. 16a) determines the output for the randomly generated critical defect parameters. The input fatigue strength scatter is independent of the failure probability. The solid points are the experimental data, as shown in Fig. 14. The empty points are the simulated data from the proposed algorithm (Fig. 11) with the fatigue strength scatter. The probabilistic modelling of selected variables correctly simulates the relationship between size effect on fatigue strength and failure probability. The difference in S_f is smaller for higher values of P_f. The trend is consistent with the experimental results (Fig. 14).
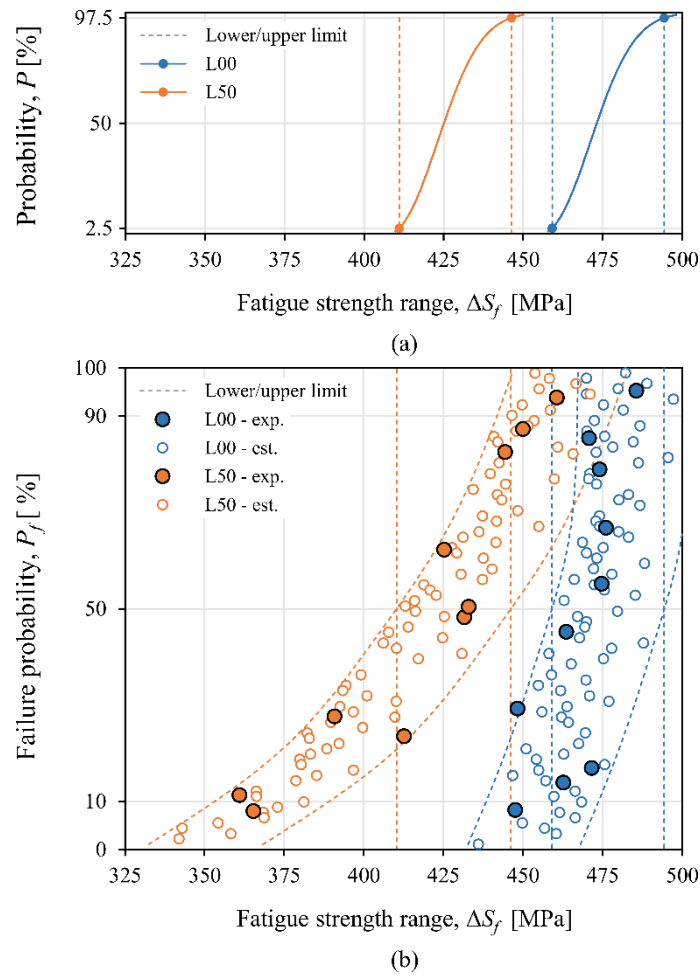

(a)

(b)

Fig. 16. Fatigue strength prediction results using linear model for normalized stress: a) input Weibull distribution, b) simulated random output and experimental data for specimens L00 and L50.

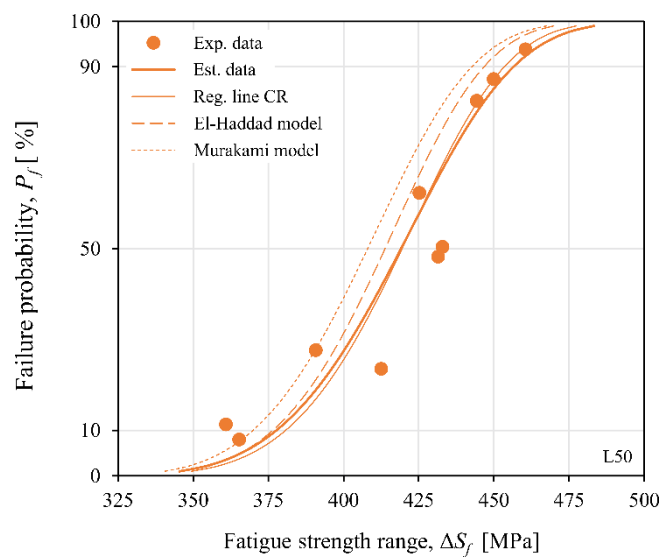Table 8. Fatigue strength prediction error for varying specimen length and failure probability.

Model		Murakami			El-Haddad			Reg. line CR		
P_f [%]		10	50	90	10	50	90	10	50	90
Specimen number	L05	3.5	2.2	1.1	1.5	1.7	1.8	0.6	0.4	1.0
	L20	6.8/4.7	5.0/2.9	3.0/1.1	3.3/1.8	3.3/1.8	3.2/1.7	2.2/0.8	2.1/0.5	2.0/1.0
	L50	1.3	2.8	4.2	0.9	1.2	3.0	0.6	0.4	0.8
Average value		3.3/2.7			2.2/1.7			1.1/0.7		
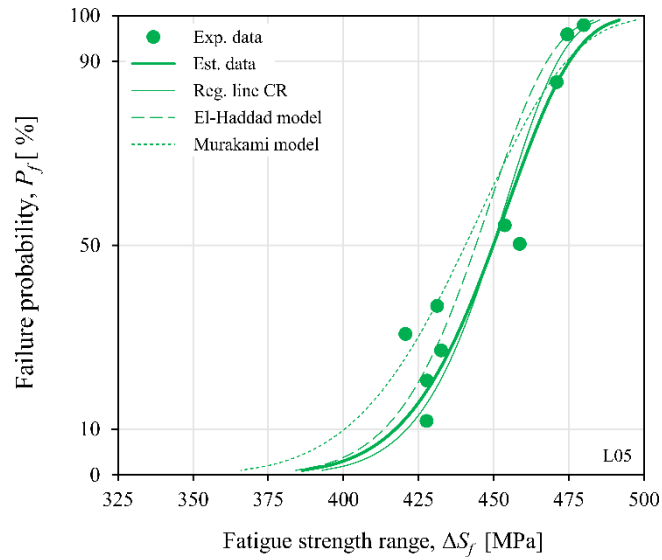
(a)
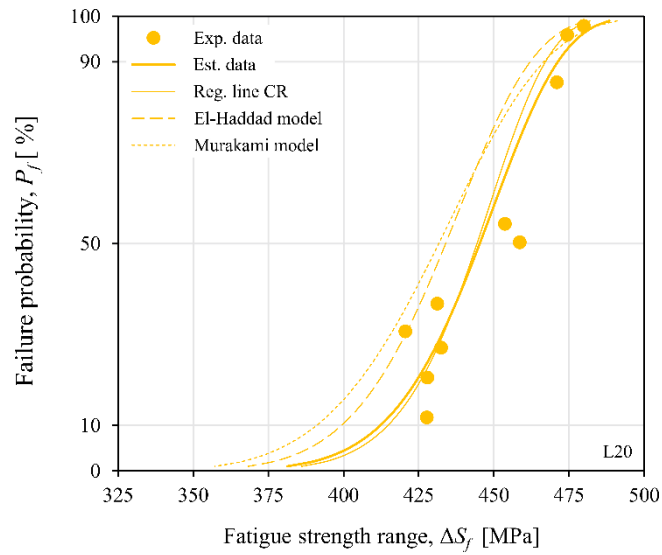
(b)

(c)

Fig. 17. Summary of Weibull cumulative distribution function of experimental and predicted fatigue strength for a R ratio of -1 and $5 \cdot 10^5$ cycles, specimen: a) L05, b) L20, c) L50.

The simulated random results were approximated by a Weibull distribution Eq. (1). The nine combinations of output data were obtained for three specimen sizes (L05, L20, L50) and three models. Table 8 shows the predicted fatigue strength for selected failure probabilities of 10%, 50%, 90% and the mean absolute percentage error. A simulation for the previously identified defect density and lower was performed for specimen L20. A subsequent analysis shows lower errors. The defect density has a significant effect on the output data. The best fit of the predicted data was obtained for the linear model for normalized stress for all specimen sizes. The average error including defect density correction for L20 is 2.7%, 1.7% and 0.7%, the Murakami model, the El-Haddad model and the regression line CR, respectively. Fig. 17 shows the cumulative distribution function for fatigue strength. The bold solid line is the estimated result for the experimental data (solid points). The thin solid and dashed lines are the output of the proposed probabilistic size effect model for all models. The results predicted using the linear model for normalized stress fit with the experimental results for probabilistic scatter bands. The Murakami and the El-Haddad models tend to underestimate the inputs.

4. Conclusion

The probabilistic size effect prediction of additively manufactured stainless steel attempts to identify a correlation between varying specimen length and fatigue strength. The direction of the studies determines the result of the failure mechanism analysis of the selected material defect parameters. The modelling of the phenomenon using analytical models has led to the following conclusions:

- The relationship between the Weibull distribution of fatigue life for variable length specimens is noticeable. The experimental data scatter increases with specimen size. The size effect on the fatigue properties of the PBF-LB 316L steel increases at lower failure probabilities. For a P_f of 10%, the estimated fatigue strength for the longest specimen (L50) decreased by 17% compared to the smallest specimen (L00).

- The analysis of the fracture surface shows the fatigue crack initiation from a single defect located in the subsurface volume of the material. Most of the defects are irregularly shaped voids with deep areas resulting from a lack of fusion. The measured defect sizes (from 53 μm to 437 μm) correlate with the fatigue properties of the PBF-LB 316L steel. An increase in the parameter $\sqrt{area}$ determines a decrease in the fatigue strength.

- A defined correlation between actual defect size and fatigue strength showed that the El-Haddad model was a better fit than the Murakami model for defects larger than 100 μm. The verified normalized Crossland stress model for the nonlocal approach around the defect determines the criticality of the subsurface defect (35% of all cases) depending on the location. The approximate linear model provides a better fit to the data than other models.

- The probabilistic approach to defect parameter scatter and the experimental data scatter resulted in the simulation of defined variables that significantly influenced the size effect prediction results. The random output of the proposed procedure was used to calculate the fatigue strength distributions using analytical models. The best fit of the predicted data was obtained for the linear model for normalized stress for all specimen sizes. The low error (less than 1%) shows the predictive validity of this model. This approach is characterised by the universality of the input variables for the defined failure measure and the fatigue properties prediction for any object size.

References

1. Haibach E. FKM – guideline – analytical strength assessment of components in mechanical engineering. VDMA Verlag 2003.
2. Hirose T, Sakasegawa H, Kohyama A, Katoh Y, Tanigawa H, 2009. Effect of specimen size on fatigue properties of reduced activation ferritic/martensitic steels. Journal of Nuclear Materials 2009;283–287:1018–1022. https://doi.org/10.1016/S0022-3115(00)00141-0
3. Kocak M, Webster S, Janosch JJ, Ainsworth RA, Koers R. FITNET Fitness-for-Service PROCEDURE – FINAL DRAFT MK7 2006.
4. Kloos KH, Buch A, Zankov D. Pure geometrical size effect in fatigue tests with constant stress amplitude and in programme tests. Materialwissenschaft und Werkstofftechnik 1981;12:40–50. https://doi.org/10.1002/mawe.19810120205
5. Makkonen M. Statistical size effect in the fatigue limit of steel. International Journal of Fatigue 2001;23:395–402. https://doi.org/10.1016/S0142-1123(01)00003-2
6. Weibull W. A statistical theory of the strength of materials. Royal Swedish Institute For Engineering Research. 1939;151.
7. Tomaszewski T. Statistical size effect in fatigue properties for mini-specimens. Materials 2020;13(10):2384. https://doi.org/10.3390/ma13102384
8. Kuguel R. A relation between theoretical stress concentration factor and fatigue notch factor deduced from the concept of highly stressed volume. ASTM 1961;61:732–748.
9. Sonsino CM, Fischer G. Local assessment concepts for the structural durability of complex loaded components. Materialwissenschaft und Werkstofftechnik 2005;36(11):632–641. https://doi.org/10.1002/mawe.200500932
10. Kaffenberger M, Vormwald M. Considering size effects in the notch stress concept for fatigue assessment of welded joints. Computational Materials Science 2012;64:71–78. https://doi.org/10.1016/j.commatsci.2012.02.047
11. Leitner M, Vormwald M, Remes H. Statistical size effect on multiaxial fatigue strength of notched steel components. International Journal of Fatigue 2017;104:322–33. https://doi.org/10.1016/j.ijfatigue.2017.08.002
12. Marques JME, Mžourek M, Papuga J, Růžička M, Benasciutti D. A probabilistic stress-life model supported by weakest link principle and highly-stressed volume/surface area concepts. International Journal of Fatigue 2024;178:108006. https://doi.org/10.1016/j.ijfatigue.2023.108006
13. Ai Y, Zhu SP, Liao D, Correia JAFO, De Jesus AMP, Keshtegar B. Probabilistic modelling of notch fatigue and size effect of components using highly stressed volume approach. International Journal of Fatigue 2019;127:110–119. https://doi.org/10.1016/j.ijfatigue.2019.06.002
14. Castillo E, Fernández-Canteli A. A unified statistical methodology for modeling fatigue damage. Springer 2009. https://doi.org/10.1007/978-1-4020-9182-7
15. Castillo E. Extreme value theory in Engineering. Academic Press 1988. https://doi.org/10.1016/C2009-0-22169-6
16. Makkonen L, Rabb R, Tikanmäki M. Size effect in fatigue based on the extreme value distribution of defects. Materials Science & Engineering A 2014;594:68–71. https://doi.org/10.1016/j.msea.2013.11.045

17. El Khoukhi D, Morel F, Saintier N, Bellett D, Osmond P, Le VD, Adrien J. Experimental investigation of the size effect in high cycle fatigue: Role of the defect population in cast aluminium alloys. International Journal of Fatigue 2019;129:105222. https://doi.org/10.1016/j.ijfatigue.2019.105222

18. Zhu S-P, Foletti S, Beretta S. Evaluation of size effect on strain-controlled fatigue behavior of a quench and tempered rotor steel: Experimental and numerical study. Materials Science & Engineering A 2018;735:423–435. https://doi.org/10.1016/j.msea.2018.08.073

19. Castillo E, López-Aenlle M, Ramos A, Fernández-Canteli A, Kieselbach R, Esslinger V. Specimen length effect on parameter estimation in modelling fatigue strength by Weibull distribution. International Journal of Fatigue 2006;28:1047–1058. https://doi.org/10.1016/j.ijfatigue.2005.11.006

20. Wang D, Volkert CA, Kraft O. Effect of length scale on fatigue life and damage formation in thin Cu films. Materials Science and Engineering A 2008;493(1–2):267–273. https://doi.org/10.1016/j.msea.2007.06.092

21. Murakami Y. Metal Fatigue: Effects of small defects and nonmetallic inclusions. Elsevier 2002. https://doi.org/10.1016/C2016-0-05272-5

22. Liang X. High cycle fatigue behavior of additive manufactured stainless steel 316L: free surface effect and microstructural heterogeneity. Materials. HESAM Université 2020.

23. Ronneberg T, Davies CM, Hooper PA. Revealing relationships between porosity, microstructure and mechanical properties of laser powder bed fusion 316L stainless steel through heat treatment. Materials & Design 2020;189:108481. https://doi.org/10.1016/j.matdes.2020.108481

24. Elangeswaran C, Cutolo A, Muralidharan GK, de Formanoir C, Berto F, Vanmeensel K, Van Hooreweder B. Effect of post-treatments on the fatigue behaviour of 316L stainless steel manufactured by laser powder bed fusion. International Journal of Fatigue 2019;123:31–39. https://doi.org/10.1016/j.ijfatigue.2019.01.013

25. ISO 6892-1:2016. Metallic Materials-Tensile Testing-Part 1: Method of Test at Room Temperature.

26. ISO-1099. Metallic Materials-Fatigue Testing-Axial Force-Controlled Method.

27. ISO-12107. Metallic Materials-Fatigue Testing-Statistical Planning and Analysis of Data.

28. Sonsino CM. Course of SN-curves especially in the high-cycle fatigue regime with regard to component design and safety. International Journal of Fatigue 2007;29(12):2246–2258. https://doi.org/10.1016/j.ijfatigue.2006.11.015

29. Andreau O, Pessard E, Koutiri I, Peyre P, Saintier N. Influence of the position and size of various deterministic defects on the high cycle fatigue resistance of a 316L steel manufactured by laser powder bed fusion. International Journal of Fatigue 2021;143:105930. https://doi.org/10.1016/j.ijfatigue.2020.105930

30. Blinn B, Krebs F, Ley M, Teutsch R, Beck T. Determination of the influence of a stress-relief heat treatment and additively manufactured surface on the fatigue behavior of selectively laser melted AISI 316L by using efficient short-time procedures. International Journal of Fatigue 2020;131:105301. https://doi.org/10.1016/j.ijfatigue.2019.105301

31. Dastgerdi JN, Jaberi O, Remes H. Influence of internal and surface defects on the fatigue performance of additively manufactured stainless steel 316L. International Journal of Fatigue 2022;163:107025. https://doi.org/10.1016/j.ijfatigue.2022.107025

32. Pessard E, Lavialle M, Laheurte P, Didier P, Brochu M. High-cycle fatigue behavior of a laser powder bed fusion additive manufactured Ti-6Al-4V titanium: Effect of pores and tested volume size. International Journal of Fatigue 2021;149:106206. https://doi.org/10.1016/j.ijfatigue.2021.106206

33. Shrestha R, Simsiriwong J, Shamsaei N. Fatigue behavior of additive manufactured 316L stainless steel parts: Effects of layer orientation and surface roughness. Additive Manufacturing 2019;28:23–38. https://doi.org/10.1016/j.addma.2019.04.011

34. Zeng F, Yang Y, Qian G. Fatigue properties and S-N curve estimating of 316L stainless steel prepared by SLM. International Journal of Fatigue 2022;162:106946. https://doi.org/10.1016/j.ijfatigue.2022.106946

35. Broek D. Elementary engineering fracture mechanics. Springer 1982. https://doi.org/10.1007/978-94-009-4333-9

36. Yadollahi A, Shamsaei N, Thompson SM, Elwany A, Bian L. Effects of building orientation and heat treatment on fatigue behavior of selective laser melted 17-4 PH stainless steel. International Journal of Fatigue 2017;94(2):218–235. https://doi.org/10.1016/j.ijfatigue.2016.03.014

37. Serrano-Munoz I, Buffiere J-Y, Mokso R, Verdu C, Nadot Y. Location, location & size: defects close to surfaces dominate fatigue crack initiation. Scientific Reports 2017;7(45239):1–9. https://doi.org/10.1038/srep45239

38. Romano S, Brückner-Foit A, Brandão A, Gumpinger J, Ghidini T, Beretta S. Fatigue properties of AlSi10Mg obtained by additive manufacturing: Defect-based modelling and prediction of fatigue

strength. Engineering Fracture Mechanics. 187, 2018, 165–189. https://doi.org/10.1016/j.engfracmech.2017.11.00

39. Tomaszewski T. Modelling of critical defect distributions for estimating the size effect of selective laser melted 316L stainless steel. International Journal of Fatigue 2023;167:107378. https://doi.org/10.1016/j.ijfatigue.2022.107378

40. Kitagawa H, Takahashi S. Fracture mechanics approach to very small crack growth and to the threshold condition. Trans Jpn Soc Mech Engng A 1979;45(399):1289–1303. https://doi.org/10.1299/kikaia.45.1289

41. Beretta S, Romano S. A comparison of fatigue strength sensitivity to defects for materials manufactured by AM or traditional processes. International Journal of Fatigue 2017;94:178–191. https://doi.org/10.1016/j.ijfatigue.2016.06.020

42. Léopold G, Nadot Y, Billaudeau T, Mendez J. Influence of artificial and casting defects on fatigue strength of moulded components in Ti-6Al-4V alloy. Fatigue and Fracture of Engineering Materials and Structures 2015;38(9):1026–1041. https://doi.org/10.1111/ffe.12326

43. Linder J, Axelsson M, Nilsson H. The influence of porosity on the fatigue life for sand and permanent mould cast aluminium. International Journal of Fatigue 2006;28(12):1752–1758. https://doi.org/10.1016/j.ijfatigue.2006.01.001

44. Houria MI, Nadot Y, Fathallah R, Roy M, Maijer DM. Influence of casting defect and SDAS on the multiaxial fatigue behaviour of A356-T6 alloy including mean stress effect. International Journal of Fatigue 2015;80:90–102. https://doi.org/10.1016/j.ijfatigue.2015.05.012

45. Romano S, Brandão A, Gumpinger J, Gschweitl M, Beretta S. Qualification of AM parts: Extreme value statistics applied to tomographic measurements. Materials & Design 2017;131:32–48. https://doi.org/10.1016/j.matdes.2017.05.091

46. El Haddad MH, Topper TH, Smith KN. Prediction of non propagating cracks. Engineering Fracture Mechanics 1979;11:573–584. https://doi.org/10.1016/0013-7944(79)90081-X

47. Taylor D. Prediction of fatigue failure location on a component using a critical distance method. International Journal of Fatigue 2000;22(9):735–742. https://doi.org/10.1016/S0142-1123(00)00062-1

48. Tomaszewski T. Nonlocal approach to fatigue analysis of a welded bicycle frame joint. Fatigue and Fracture of Engineering Materials and Structures 2023;46(9):3179–3192. https://doi.org/10.1111/ffe.14066

49. Wilson P, Saintier N, Palin-Luc T, Sudret B, Bergamo S. Statistical study of the size and spatial distribution of defects in a cast aluminium alloy for the low fatigue life assessment. International Journal of Fatigue 2023;166:107206. https://doi.org/10.1016/j.ijfatigue.2022.107206

50. Romano S, Miccoli S, Beretta S. A new FE post-processor for probabilistic fatigue assessment in the presence of defects and its application to AM parts. International Journal of Fatigue 2019;125:324–341. https://doi.org/10.1016/j.ijfatigue.2019.04.008

51. Crossland B. Effect of large hydrostatic pressures on the torsional fatigue strength of fan alloy steel. Proceedings Of The International Conference On Fatigue Of Metals 1956:138–149.

52. Bonneric M, Brugger C, Saintier N. Investigation of the sensitivity of the fatigue resistance to defect position in aluminium alloys obtained by Selective laser melting using artificial defects. International Journal of Fatigue 2020;134:105505. https://doi.org/10.1016/j.ijfatigue.2020.105505

53. El May M, Saintier N, Palin-Luc T, Devos O. Non-local high cycle fatigue strength criterion for metallic materials with corrosion defects. Fatigue and Fracture of Engineering Materials and Structures 2015;38(9):1017–1025. https://doi.org/10.1111/ffe.12329

54. Mu P, Nadot Y, Nadot-Martin C, Chabod A, Serrano-Munoz I, Verdu C. Influence of casting defects on the fatigue behavior of cast aluminum AS7G06-T6. International Journal of Fatigue 2014;63:97–109. https://doi.org/10.1016/j.ijfatigue.2014.01.011

55. Papadopoulos IV, Avoli P, Gorla C, Filippini M, Bernasconi A. A comparative study of multiaxial high-cycle fatigue criteria for metals. International Journal of Fatigue 1997;19(3):219–235. https://doi.org/10.1016/S0142-1123(96)00064-3

56. Wallin K. Statistical aspects of fatigue life and endurance limit. Fatigue and Fracture of Engineering Materials and Structures 2010;33(6):333–344. https://doi.org/10.1111/j.1460-2695.2010.01445.x

57. Furuya Y. Notable size effects on very high cycle fatigue properties of high-strength steel. Materials Science and Engineering A 2011;528:5234–5240. https://doi.org/10.1016/j.msea.2011.03.082

58. Tomaszewski T, Sempruch J. Determination of the fatigue properties of aluminum alloy using mini specimen. Fatigue Failure and Fracture Mechanics 2012;726:63–68. https://doi.org/10.4028/www.scientific.net/MSF.726.63